THE JOURNAL OF PHYSICAL CHEMISTRY Letters

Cite This: J. Phys. Chem. Lett. 2019, 10, 7−12

Letter

pubs.acs.org/JPCL

Two-Dimensional Lead-Free Perovskite $(C_6H_5C_2H_4NH_3)_2CsSn_2I_7$ with High Hole Mobility

Hongzhi Shen,[†] Junze Li,[†] Haizhen Wang,[‡] Jiaqi Ma,[†] Jun Wang,[†] Hongmei Luo,[‡] and Dehui Li*[,†]

[†]School of Optical and Electronic Information and Wuhan National Laboratory for Optoelectronics, Huazhong University of Science and Technology, Wuhan 430074, China

[‡]Department of Chemical and Materials Engineering, New Mexico State University, Las Cruces, New Mexico 88003, United States

Supporting Information

ABSTRACT: Two-dimensional (2D) organic−inorganic perovskites have recently undergone rapid development because of their unique optical properties, layered nature, and better environmental stability. Here, we report on a new type of 2D lead-free perovskite $(C_6H_5C_2H_4NH_3)_2CsSn_2I_7$ crystals with millimeter size and high field-effect hole mobility synthesized by a solution method. The excellent crystalline quality and phase purity have been verified by X-ray diffraction and low-temperature photoluminescence studies, while the X-ray photoelectron spectroscopy and energy-dispersive spectrometry measurements reveal the successful incorporation of Cs element into the resultant crystals and the absence of Sn^{4+} in the as-synthesized crystals. The as-synthesized crystals exhibit a high electrical conductivity and a high hole mobility up to 34 $cm^2 \cdot V^{-1} \cdot s^{-1}$ at 77 K. The crystals also show a high photoresponse resulting from the excellent optical properties and high electrical conductivity. Our findings show that the lead-free $(C_6H_5C_2H_4NH_3)_2CsSn_2I_7$ crystals with excellent optoelectronic properties would be a promising material for electronic and optoelectronic applications.

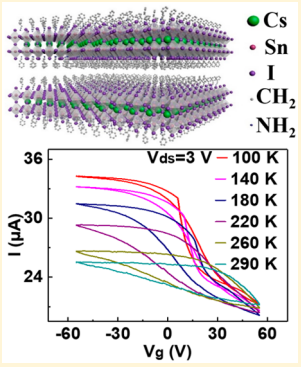

Conventional three-dimensional (3D) hybrid organic−inorganic perovskites have emerged as a new type of high-performance semiconductors over the past few years and attracted extensive studies for their promising optoelectronic applications, such as solar cells,[1−4] photodetectors,[5,6] lasers,[7−10] and light-emitting devices.[11−13] In particular, the certified power conversion efficiency of Pb-based halide perovskite solar cells has currently soared up to above 23% within a very short period of time,[1] which renders the perovskite-based solar cells tremendously promising for photovoltaic applications. However, 3D perovskites exhibit extreme instability against moisture, light, and heating and are very toxic with the presence of lead, which severely hinder their commercialization.[14] Two-dimensional (2D) Ruddlesden−Popper perovskites can significantly improve the long-term environmental stability because of the presence of the hydrophobicity of the organic chain which can prevent the inorganic layer from being directly contacted with moisture in air,[15] while the toxicity of the lead in perovskite materials can be resolved by replacing the lead with less toxic or nontoxic metals such as bismuth (Bi),[16] germanium (Ge),[17] and tin (Sn).[18,19] Therefore, it is expected that 2D Sn-based perovskites[20−22] could simultaneously address both the environmental stability and toxicity of the lead and thus have attracted extensive attention recently.

Considerable effort has been invested, and some breakthroughs have been achieved in Sn-based 3D perovskite solar cells in the past few years. The maximum power conversion efficiency of Sn-based perovskite solar cells can reach 10.2%[23] in the planar p-i-n structures, and increasing research effort is continuously being devoted to this field for further improvement of the device performance. Nevertheless, the instability of Sn-based perovskites due to the easy oxidation of Sn^{2+} to Sn^{4+} hinders their application in practice.[24] Although the oxidation of Sn^{2+} to Sn^{4+} leads to self-doping and thus the improved electrical conductivity of the Sn-based perovskites, the oxidation would shorten the lifetime of devices.[18−20,24,25]

Two-dimensional Sn-based perovskites with better environmental stability have also drawn great attention, and the electrical conductivity and optical properties of layered $(C_4H_9NH_3)_2(CH_3NH_3)_{n-1}Sn_nI_{3n+1}$ series (n = 1, 2, 3, 4, 5, and ∞) have been investigated.[22] 2D Sn-based perovskite solar cells have achieved a power conversion efficiency of 5.94%[22] with enhanced environmental stability. In addition, thin-film transistors based on $(PEA)_2SnI_4$ films produced by the spin-coating method were first reported in 1999,[26] and the performance of the transistors has been greatly improved by using a melt-processed method,[27] resulting in a mobility of ∼2.6 $cm^2 \cdot V^{-1} \cdot s^{-1}$. To date, the carrier mobility of a $(PEA)_2SnI_4$-based transistor can reach as high as 15 $cm^2 \cdot V^{-1} \cdot s^{-1}$ by using an MoO_3 layer as the electrode material.[21] Particularly, it is revealed that 2D perovskites with a greater layer number n would give a better electrical conductivity[28] and that Cs-based perovskites would be able to further improve the stability of the perovskite materials.[29,30] To this end, we expect that the Sn- and Cs-based 2D perovskites with a

Received: November 6, 2018
Accepted: December 17, 2018
Published: December 17, 2018

DOI: 10.1021/acs.jpclett.8b03381
J. Phys. Chem. Lett. 2019, 10, 7−12

large layer number n would exhibit both improved electronic and optical properties with great air stability; nevertheless, this has largely not been explored yet.

Here, we have for the first time successfully synthesized Sn- and Cs-based 2D hybrid organic−inorganic perovskite $(PEA)_2CsSn_2I_7$ (PEA= $C_6H_5C_2H_4NH_3$) crystals with millimeter size. X-ray diffraction (XRD) and temperature-dependent photoluminescence (PL) studies reveal the high purity and excellent crystalline quality of the as-synthesized $(PEA)_2CsSn_2I_7$ crystals, whereas X-ray photoelectron spectroscopy (XPS) measurement indicates the absence of Sn^{4+} in our samples,[31] which is critical for the electronic and optoelectronic applications.[19,20,24,25] Electrical measurement shows that the as-synthesized samples are p-type semiconductors with a high electrical conductivity and a high field-effect hole mobility of 34 $cm^2 \cdot V^{-1} \cdot s^{-1}$ at 77 K. The as-synthesized $(PEA)_2CsSn_2I_7$ crystals also exhibit excellent photoresponse, as supported by the photoconductivity (PC) measurement.

The schematic illustration of the crystal structure of $(PEA)_2CsSn_2I_7$ is shown in Figure 1a, which presents that

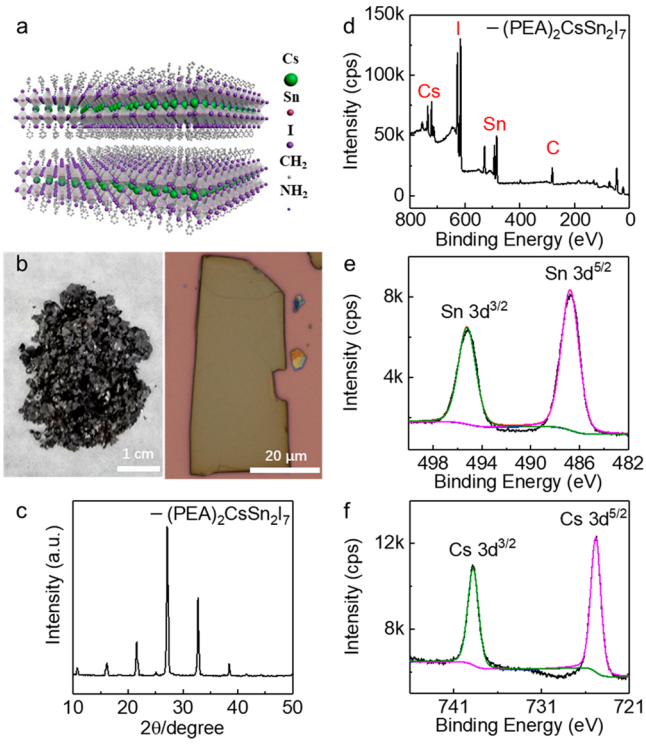

Figure 1. (a) Schematic illustration of the crystal structure of $(PEA)_2CsSn_2I_7$ perovskite. (b) Photograph and OM image of the as-synthesized $(PEA)_2CsSn_2I_7$ perovskite crystals. XRD (c) and XPS (d) spectra of the as-prepared $(PEA)_2CsSn_2I_7$ perovskite crystals. Zoom-in XPS spectra of $3d^{3/2}$ and $3d^{5/2}$ of Sn (e) and Cs (f) elements.

the double corner-sharing $[SnI_6]^{4-}$ octahedra layers are sandwiched between two layers of the long-chain organic molecules via van der Waals forces.[15,32] Figure 1b displays the optical microscopy (OM) image of the as-synthesized $(PEA)_2CsSn_2I_7$ crystals, which have millimeter size and black color. The layered nature of $(PEA)_2CsSn_2I_7$ allows us to mechanically exfoliate thin flakes from their bulk counterparts and further fabricate microdevices and integrate with other layered materials to extend their functionalities.[32,33] The right panel of Figure 1b shows one piece of the exfoliated flake with a rather smooth surface, which would be beneficial for making devices and stacked heterostructures.[32] The powder XRD pattern of the as-synthesized $(PEA)_2CsSn_2I_7$ crystals (Figure 1c) exhibits very strong main peaks with narrow full width at half-maximum (FWHM), suggesting the excellent crystalline quality of the samples.[33]

As previously reported, Sn element is susceptible to being oxidized in ambient conditions, which will promote the formation of Sn^{2+} vacancies and thus lead to degenerately doped Sn-based perovskites, shortening the lifetime of the devices based on Sn-based perovskites.[19,20,24,25] To confirm whether there is Sn^{4+} within the as-synthesized $(PEA)_2CsSn_2I_7$ crystals,[31] XPS measurement was carried out as shown in Figure 1d−f, which suggests that C, Sn, I, and Cs elements are present in the as-synthesized crystals, consistent with that of energy-dispersive spectrometry (EDS) measurement (Figure S1a). The presence of the Cs element confirms that the Cs is indeed inserted into the double $[SnI_6]^{4-}$ octahedra (Figure 1f). Close inspection of Sn (3d) shows that two peaks are present with the binding energy of 495.2 and 486.8 eV (Figure 1e),[34] which clearly indicates the absence of Sn^{4+} in our samples. This might be due to the excess strong reducing H_3PO_2 solution we used during the growth process,[20] which can efficiently suppress the Sn^{2+} from being oxidized to Sn^{4+}.

To investigate the optical properties of the as-synthesized $(PEA)_2CsSn_2I_7$ crystals, temperature-dependent PL studies have been carried out on the exfoliated microplates. The as-prepared microplates were immediately put into the vacuum chamber to avoid sample degradation.[14] While only one emission peak located at 700 nm was observed at room temperature, two distinct peaks located at 725 and 735 nm were present at 77 K, which might be assigned to the free exciton and bound exciton emission, respectively (Figure 2a).[35] The absence of any defect emission at 77 K suggests the high quality of the as-synthesized samples.

To clarify the origins of these two emission peaks, we have carried out temperature-dependent (Figure 2b) and power-dependent photoluminescence spectra at 77 K (Figure S2). The steady-state temperature-dependent PL mapping of a $(PEA)_2CsSn_2I_7$ thin flake excited by a 473 nm laser shows that two emission peaks are clearly distinguished for temperature below 140 K and that only one is observed above 140 K. As the temperature increases, the lower-energy emission peak fades away while the higher-energy emission peak shows a gradually blue-shift, similar to 3D perovskites.[36−38] This also supports our assignment that the lower-energy emission peak originates from the bound exciton emission while the higher-energy one originates from free exciton emission. The power-dependent PL spectra at 77 K indicates that the intensity of both emission peaks shows a linear increase with the excitation power in the range we investigated but with a different slope, which suggests those two emission peaks have different origins (Figure S2). Because the higher-energy emission peak can be unambiguously ascribed to the free exciton emission from the temperature-dependent PL spectra (Figure 2b), we can further confirm that the lower-energy one is due to the bound exciton emission based on the power-dependent PL intensity. Nevertheless, our samples are easily damaged under a high excitation power even at 77 K, and thus we did not observe the intensity saturation.[39]

The emission peak positions and FWHMs were extracted from Figure 2b and plotted against temperature (Figure 2c).

DOI: 10.1021/acs.jpclett.8b03381
J. Phys. Chem. Lett. 2019, 10, 7−12

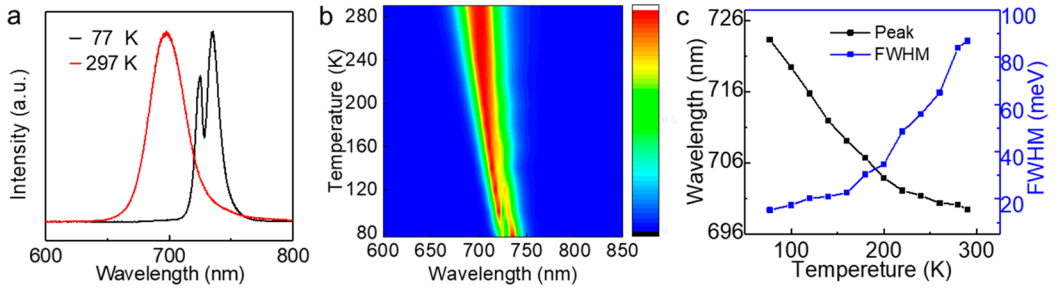

Figure 2. (a) Photoluminescence (PL) spectra at room temperature and 77 K. (b) Temperature-dependent PL map of a $(PEA)_2CsSn_2I_7$ microplate measured in a 20 K step. (c) Temperature-dependent emission peak and the full width at half-maximum (FWHM) of free exciton emission peak extracted from panel b.

The emission peak continuously blue-shifts, and the fwhm gradually broadens with the increasing temperature, which can be ascribed to the enhanced electron−phonon interaction at higher temperatures as previously reported.[36−38]

The layered nature of $(PEA)_2CsSn_2I_7$ crystals enables us to fabricate microplate electronic devices via transferring exfoliated flakes to prefabricated two-probe electrodes to investigate the electronic properties of the as-synthesized $(PEA)_2CsSn_2I_7$ crystals, which is essential for improving the performance of optoelectronic devices.[32] Figure 3a displays the

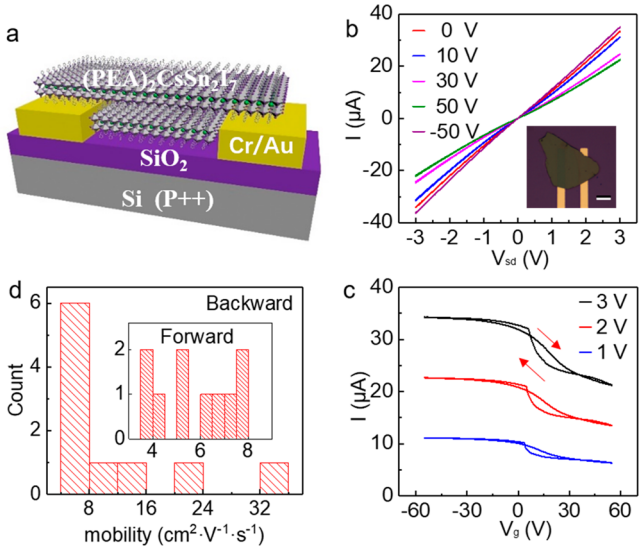

Figure 3. (a) Schematic illustration of the exfoliated $(PEA)_2CsSn_2I_7$ microplate device. (b) Output characteristics of the exfoliated $(PEA)_2CsSn_2I_7$ microplate device under various gate voltages at 77 K. The inset shows the OM image of the device, with a scale bar of 20 μm. (c) Transfer characteristics of the exfoliated $(PEA)_2CsSn_2I_7$ microplate device under different biases at 77 K. (d) Statistical histogram of the hole mobility of 10 different devices for both the forward and backward sweepings under a bias of 3 V.

schematic illustration of a bottom-gate, bottom-contact $(PEA)_2CsSn_2I_7$ thin-flake transistor on a 300 nm SiO_2/Si substrate with a channel length of 20 μm and 300 nm SiO_2 working as the dielectric layer. Predefined 5 nm Cr/50 nm Au symmetric electrodes are used to avoid the lithography process which would damage the perovskite flakes.[40] The optical image of a typical flake device suggests that the surface of the exfoliated flake is very smooth (inset of Figure 3b). The as-prepared devices are immediately put into the vacuum chamber to minimize the degradation in air.[14] All electrical measurements are carried out in dark.

Figure 3b displays the output characteristics of a typical $(PEA)_2CsSn_2I_7$ thin flake transistor under different back-gate voltages at 77 K. The linearity of the I_{sd} versus V_{sd} curves indicates the Ohmic contact formed between the Au and the perovskite flake.[41] The source−drain current I_{sd} continuously increases with the decreasing gate voltage V_g, suggesting a p-type semiconductor behavior. The transfer characteristics further confirm that the as-synthesized $(PEA)_2CsSn_2I_7$ crystals are p-type semiconductors (Figure 3c). A small hysteresis has been observed for all transfer curves at 77 K, which might be due to the ferroelectricity and/or charge trapping and detrapping because the ion migration has proven to be greatly suppressed in 2D perovskites,[42] unlike their 3D counterparts.[43,44] Interestingly, there was a crossing in the hysteresis at 77 K, the possible origin of which will be discussed below. The transfer curves cannot be fully switched off (Figure 3c), probably resulting from the high carrier concentration in our as-synthesized samples, which makes the $(PEA)_2CsSn_2I_7$ crystals be nearly degenerate semiconductors, leading to the metallic properties as previously reported.[45]

The field-effect hole mobility μ was extracted by using the formula $\mu = \frac{L}{WCV_{sd}}\frac{dI_{sd}}{dV_g}$, where L is the channel length, W the channel width, C the gate-channel capacitance, V_{sd} the source−drain voltage, I_{sd} the source−drain current, and V_g the gate-voltage. The capacitance of SiO_2 was calculated according to the parallel-plate capacitor model, which is estimated to be 11.5 nF/cm^2 in our case.[46] Because of the presence of the hysteresis, the mobility values are extracted from both the forward and backward sweeping of the transfer characteristics. Figure 3d exhibits the statistical histogram of the hole mobility for 10 different devices for both the forward and backward sweepings under a bias of 3 V at 77 K. The average mobility for forward and backward sweeping are 11.6 and 5.8 cm^2·V^{-1}·s^{-1}, respectively. Remarkably, the mobility can achieve as high as 34 cm^2·V^{-1}·s^{-1} for backward sweeping, which is the highest value in 2D perovskites to date.[47]

Temperature-dependent electrical measurement has been carried out to understand the underlying charge transport mechanism.[48,49] The source−drain current I_{sd} increases linearly with the applied source−drain voltage V_{sd} under a gate voltage of 0 V for all temperatures we investigated (Figure 4a), suggesting the excellent electrical contact for our devices.[41] The source−drain current I_{sd} continuously decreases as the temperature increases (Figure 4a). A similar temperature-dependent source−drain current I_{sd} was also observed in the transfer curve (Figure 4b). Nevertheless, the hysteresis in the

DOI: 10.1021/acs.jpclett.8b03381
J. Phys. Chem. Lett. 2019, 10, 7−12

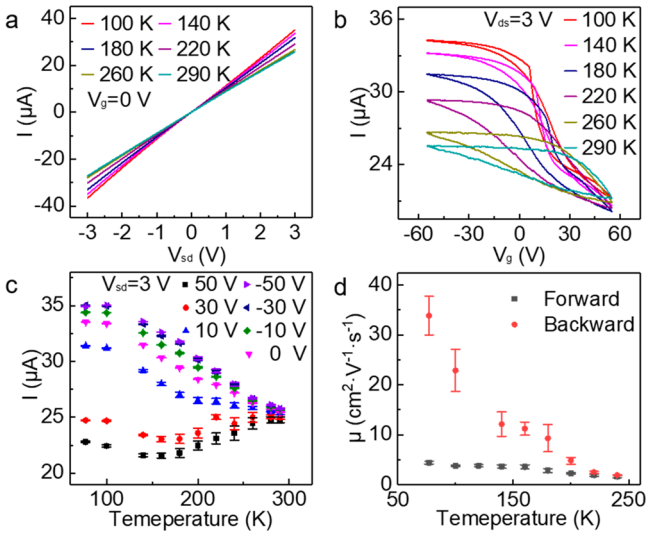

Figure 4. Temperature-dependent output (a) and transfer (b) characteristics of a exfoliated $(PEA)_2CsSn_2I_7$ microplate device. (c) Temperature-dependent source−drain current under different gate voltages. (d) Temperature evolution of the field-effect hole mobility extracted from both forward and backward sweepings.

I_{sd}−V_g curves increases with the increase of the temperature, suggesting the charge trapping and detrapping play the dominant role in the hysteresis observed here.[50] Meanwhile, similar to the 77 K case, the crossing in the hysteresis has also been observed at 100 K and disappeared with further increasing temperature. The crossing in the hysteresis also depends on the interface, which is absent for the devices on Si_3N_4 substrates (Figure S3). Therefore, this crossing is very likely to be due to the charge trapping at the interface.

The temperature-dependent source−drain current I_{sd} under different gate voltages V_g was extracted and plotted against temperature as shown in Figure 4c. Under large positive gate voltages, the source−drain current I_{sd} first decreases and then increases with the decreasing temperature while the source−drain current I_{sd} continuously increases as the temperature decreases for the negative and small positive gate voltages (Figure 4c). The evolution of the source−drain current I_{sd} with varying the gate voltages might be ascribed to the gate voltage-induced Fermi level shift,[51] leading to the insulator-to-bandlike transport transition, similar to the 3D perovskite case.[52] Similar results have been observed on Si_3N_4 substrate (Figure S3), indicating that the observed evolution of the source−drain current I_{sd} with temperature is not due to extrinsic factors, such as perovskite−substrate interface.[53] In contrast to the temperature-dependent source−drain current I_{sd}, the extracted hole mobility for both forward and backward sweeping continuously increases with the decrease of the temperature (Figure 4d) because of the reduced electron−phonon interaction at lower temperatures.[48,49,54] Due to the huge hysteresis at room temperature, the calculated field-effect mobility is not accurate, and thus, we did not include the mobility at room temperature in Figure 4d.

The $(PEA)_2CsSn_2I_7$ microplate-based two-probe device also exhibits excellent photoresponse. Under white light illumination, the source−drain current increases from around 4 to 8 μA at a source−drain voltage of 1 V (Figure S4a), corresponding to a responsivity of ∼1250 A/W, which is much larger than that of 2D Pb-based photodetectors.[55,56] The photoresponse was also confirmed by the optical switch characteristics (Figure S4b), which shows rapid current rise and fall with switching on and off the light. We believe that the photoresponse performance can be further improved with optimizing the device structures.

In summary, we have successfully synthesized a new type of lead-free 2D perovskite $(PEA)_2CsSn_2I_7$ crystals with millimeter size. XRD and low temperature-dependent PL studies reveal the excellent crystalline quality and phase purity of the as-synthesized crystals. EDS and XPS measurement confirm the successful incorporation of Cs into the crystals and the absence of the Sn^{4+} ions due to the usage of the strong reducing H_3PO_2 solution during the synthesis process. The electrical measurement indicates the as-synthesized samples have high electrical conductivity and undergo the insulator-to-bandlike transport transition tuned by the applied gate voltage. The field-effect hole mobility can achieve values as high as 34 $cm^2 \cdot V^{-1} \cdot s^{-1}$, whereas the strong photoresponse was verified by photoconductivity measurement. Our findings suggest that this new 2D perovskite might find promising optoelectronic applications because of its excellent optical and electronic properties.

■ ASSOCIATED CONTENT

Supporting Information

The Supporting Information is available free of charge on the ACS Publications website at DOI: 10.1021/acs.jpclett.8b03381.

EDS and supplementary XPS spectrum, temperature-dependent electrical measurements of the 2D perovskite microplate transistors on Si_3N_4 substrates, photoresponse characteristics, power-dependent PL spectra, and the experimental methods (PDF)

■ AUTHOR INFORMATION

Corresponding Author

*E-mail: dehuili@hust.edu.cn.

ORCID

Hongmei Luo: 0000-0002-9546-761X

Dehui Li: 0000-0002-5945-220X

Notes

The authors declare no competing financial interest.

■ ACKNOWLEDGMENTS

D.L. acknowledges the support from NSFC (61674060) and the Fundamental Research Funds for the Central Universities, HUST (2017KFYXJJ030, 2017KFXKJC002, 2017KFXKJC003, and 2018KFYXKJC016); H.L. acknowledges the support from New Mexico EPSCoR with NSF-1301346. We thank Hong Cheng, engineer in the Analytical and Testing Center of Huazhong University of Science and Technology, for the support in PL measurement and thank the Center of Micro-Fabrication of WNLO for the support in device fabrication.

■ REFERENCES

(1) NREL. Best research-cell efficiencies. https://www.nrel.Gov/pv/assets/images/efficiency-chart-20180716.jpg (accessed July 16, 2018).

(2) Lee, M. M.; Teuscher, J.; Miyasaka, T.; Murakami, T. N.; Snaith, H. J. Efficient hybrid solar cells based on meso-superstructured organometal halide perovskites. *Science* **2012**, *338*, 643−647.

(3) Nie, W.; Tsai, H.; Asadpour, R.; Blancon, J.-C.; Neukirch, A. J.; Gupta, G.; Crochet, J. J.; Chhowalla, M.; Tretiak, S.; Alam, M. A.;

DOI: 10.1021/acs.jpclett.8b03381
J. Phys. Chem. Lett. 2019, 10, 7−12

et al. High-efficiency solution-processed perovskite solar cells with millimeter-scale grains. *Science* **2015**, *347*, 522−525.
(4) Yin, W.-J.; Yang, J.-H.; Kang, J.; Yan, Y.; Wei, S.-H. Halide perovskite materials for solar cells: a theoretical review. *J. Mater. Chem. A* **2015**, *3*, 8926−8942.
(5) Wang, Y.; Fullon, R.; Acerce, M.; Petoukhoff, C. E.; Yang, J.; Chen, C.; Du, S.; Lai, S. K.; Lau, S. P.; Voiry, D.; O'Carroll, D.; et al.et. al Solution-processed MoS_2 /organolead trihalide perovskite photodetectors. *Adv. Mater.* **2017**, *29*, 1603995.
(6) Dou, L.; Yang, Y. M.; You, J.; Hong, Z.; Chang, W. H.; Li, G.; Yang, Y. Solution-processed hybrid perovskite photodetectors with high detectivity. *Nat. Commun.* **2014**, *5*, 5404.
(7) Zhu, H.; Fu, Y.; Meng, F.; Wu, X.; Gong, Z.; Ding, Q.; Gustafsson, M. V.; Trinh, M. T.; Jin, S.; Zhu, X. Y. Lead halide perovskite nanowire lasers with low lasing thresholds and high quality factors. *Nat. Mater.* **2015**, *14*, 636−642.
(8) Xing, G.; Mathews, N.; Lim, S. S.; Yantara, N.; Liu, X.; Sabba, D.; Gratzel, M.; Mhaisalkar, S.; Sum, T. C. Low-temperature solution-processed wavelength-tunable perovskites for lasing. *Nat. Mater.* **2014**, *13*, 476−480.
(9) Zhang, Q.; Su, R.; Du, W.; Liu, X.; Zhao, L.; Ha, S. T.; Xiong, Q. Advances in small perovskite-based lasers. *Small Methods* **2017**, *1*, 1700163.
(10) Su, R.; Diederichs, C.; Wang, J.; Liew, T. C. H.; Zhao, J.; Liu, S.; Xu, W.; Chen, Z.; Xiong, Q. Room-temperature polariton lasing in all-inorganic perovskite nanoplatelets. *Nano Lett.* **2017**, *17*, 3982−3988.
(11) Cao, Y.; Wang, N.; Tian, H.; Guo, J.; Wei, Y.; Chen, H.; Miao, Y.; Zou, W.; Pan, K.; He, Y.; et al. Perovskite light-emitting diodes based on spontaneously formed submicrometre-scale structures. *Nature* **2018**, *562*, 249−253.
(12) Lin, K.; Xing, J.; Quan, L. N.; de Arquer, F. P. G.; Gong, X.; Lu, J.; Xie, L.; Zhao, W.; Zhang, D.; Yan, C.; et al. Perovskite light-emitting diodes with external quantum efficiency exceeding 20%. *Nature* **2018**, *562*, 245−248.
(13) Xing, J.; Zhao, Y.; Askerka, M.; Quan, L. N.; Gong, X.; Zhao, W.; Zhao, J.; Tan, H.; Long, G.; Gao, L.; Yang, Z.; Voznyy, O.; Tang, J.; Lu, Z.-H.; Xiong, Q.; Sargent, E. H. Color-stable highly luminescent sky-blue perovskite light-emitting diodes. *Nat. Commun.* **2018**, *9*, 3541.
(14) Rong, Y.; Liu, L.; Mei, A.; Li, X.; Han, H. Beyond efficiency: the challenge of stability in mesoscopic perovskite solar cells. *Adv. Energy Mater.* **2015**, *5*, 1501066.
(15) Chen, Y.; Sun, Y.; Peng, J.; Tang, J.; Zheng, K.; Liang, Z. 2D Ruddlesden-Popper perovskites for optoelectronics. *Adv. Mater.* **2018**, *30*, 1703487.
(16) Singh, T.; Kulkarni, A.; Ikegami, M.; Miyasaka, T. Effect of electron transporting layer on bismuth-based lead-free perovskite $(CH_3NH_3)_3Bi_2I_9$ for photovoltaic applications. *ACS Appl. Mater. Interfaces* **2016**, *8*, 14542−14547.
(17) Stoumpos, C. C.; Frazer, L.; Clark, D. J.; Kim, Y. S.; Rhim, S. H.; Freeman, A. J.; Ketterson, J. B.; Jang, J. I.; Kanatzidis, M. G. Hybrid germanium iodide perovskite semiconductors: active lone pairs, structural distortions, direct and indirect energy gaps, and strong nonlinear optical properties. *J. Am. Chem. Soc.* **2015**, *137*, 6804−6819.
(18) Ke, W.; Stoumpos, C. C.; Kanatzidis, M. G. "Unleaded" perovskites: status quo and future prospects of tin-based perovskite solar cells. *Adv. Mater.* **2018**, No. 1803230.
(19) Konstantakou, M.; Stergiopoulos, T. A critical review on tin halide perovskite solar cells. *J. Mater. Chem. A* **2017**, *5*, 11518−11549.
(20) Cao, D. H.; Stoumpos, C. C.; Yokoyama, T.; Logsdon, J. L.; Song, T.-B.; Farha, O. K.; Wasielewski, M. R.; Hupp, J. T.; Kanatzidis, M. G. Thin films and solar cells based on semiconducting two-dimensional Ruddlesden−Popper $(CH_3(CH_2)_3NH_3)_2(CH_3NH_3)_{n-1}Sn_nI_{3n+1}$ perovskites. *ACS Energy Lett.* **2017**, *2*, 982−990.
(21) Matsushima, T.; Hwang, S.; Sandanayaka, A. S.; Qin, C.; Terakawa, S.; Fujihara, T.; Yahiro, M.; Adachi, C. Solution-processed organic-inorganic perovskite field-effect transistors with high hole mobilities. *Adv. Mater.* **2016**, *28*, 10275−10281.
(22) Liao, Y.; Liu, H.; Zhou, W.; Yang, D.; Shang, Y.; Shi, Z.; Li, B.; Jiang, X.; Zhang, L.; Quan, L. N.; et al. Highly oriented low-dimensional tin halide perovskites with enhanced stability and photovoltaic performance. *J. Am. Chem. Soc.* **2017**, *139*, 6693−6699.
(23) Chung, I.; Lee, B.; He, J.; Chang, R. P.; Kanatzidis, M. G. All-solid-state dye-sensitized solar cells with high efficiency. *Nature* **2012**, *485*, 486−489.
(24) Chung, I.; Song, J. H.; Im, J.; Androulakis, J.; Malliakas, C. D.; Li, H.; Freeman, A. J.; Kenney, J. T.; Kanatzidis, M. G. $CsSnI_3$: Semiconductor or metal? High electrical conductivity and strong near-infrared photoluminescence from a single material. High hole mobility and phase-transitions. *J. Am. Chem. Soc.* **2012**, *134*, 8579−8587.
(25) Stoumpos, C. C.; Malliakas, C. D.; Kanatzidis, M. G. Semiconducting tin and lead iodide perovskites with organic cations: phase transitions, high mobilities, and near-infrared photoluminescent properties. *Inorg. Chem.* **2013**, *52*, 9019−9038.
(26) Kagan, C. R.; Mitzi, D. B.; Dimitrakopoulos, C. D. Organic-inorganic hybrid materials as semiconducting channels in thin-film field-effect transistors. *Science* **1999**, *286*, 945−947.
(27) Mitzi, D. B.; Dimitrakopoulos, C. D.; Rosner, J.; Medeiros, D. R.; Xu, Z.; Noyan, C. Hybrid field-effect transistor based on a low-temperature melt-processed channel layer. *Adv. Mater.* **2002**, *14*, 1772−1776.
(28) Mitzi, D. B.; Feild, C. A.; Harrison, W. T. A.; Guloy, A. M. Conducting tin halides with a layered organic-based perovskite strucyure. *Nature* **1994**, *369*, 467−469.
(29) Saliba, M.; Matsui, T.; Seo, J. Y.; Domanski, K.; Correa-Baena, J. P.; Nazeeruddin, M. K.; Zakeeruddin, S. M.; Tress, W.; Abate, A.; Hagfeldt, A.; et al. Cesium-containing triple cation perovskite solar cells: improved stability, reproducibility and high efficiency. *Energy Environ. Sci.* **2016**, *9*, 1989−1997.
(30) Lee, J.; Kim, D.; Kim, H.; Seo, S.; Cho, S. M.; Park, N. Formamidinium and cesium hybridization for photo- and moisture-stable perovskite solar cell. *Adv. Energy Mater.* **2015**, *5*, 1501310.
(31) Choi, W. K.; Jung, H. J.; Koh, S. K. Chemical shifts and optical properties of tin oxide films grown by a reactive ion assisted deposition. *J. Vac. Sci. Technol., A* **1996**, *14*, 359−366.
(32) Geim, A. K.; Grigorieva, I. V. Van der Waals heterostructures. *Nature* **2013**, *499*, 419−425.
(33) Stoumpos, C. C.; Cao, D. H.; Clark, D. J.; Young, J.; Rondinelli, J. M.; Jang, J. I.; Hupp, J. T.; Kanatzidis, M. G. Ruddlesden−Popper hybrid lead iodide perovskite 2D homologous semiconductors. *Chem. Mater.* **2016**, *28*, 2852−2867.
(34) Willemen, H.; Van De Vondel, D. F.; Van Der Kelen, G. P. An ESCA study of tin compounds. *Inorg. Chim. Acta* **1979**, *34*, 175−180.
(35) Straus, D. B.; Hurtado Parra, S.; Iotov, N.; Gebhardt, J.; Rappe, A. M.; Subotnik, J. E.; Kikkawa, J. M.; Kagan, C. R. Direct observation of electron-phonon coupling and slow vibrational relaxation in organic-inorganic hybrid perovskites. *J. Am. Chem. Soc.* **2016**, *138*, 13798−13801.
(36) Wright, A. D.; Verdi, C.; Milot, R. L.; Eperon, G. E.; Perez-Osorio, M. A.; Snaith, H. J.; Giustino, F.; Johnston, M. B.; Herz, L. M. Electron-phonon coupling in hybrid lead halide perovskites. *Nat. Commun.* **2016**, *7*, 11755.
(37) Chen, Z.; Yu, C.; Shum, K.; Wang, J. J.; Pfenninger, W.; Vockic, N.; Midgley, J.; Kenney, J. T. Photoluminescence study of polycrystalline $CsSnI_3$ thin films: Determination of exciton binding energy. *J. Lumin.* **2012**, *132*, 345−349.
(38) Ni, L.; Huynh, U.; Cheminal, A.; Thomas, T. H.; Shivanna, R.; Hinrichsen, T. F.; Ahmad, S.; Sadhanala, A.; Rao, A. Real-time observation of exciton-phonon coupling dynamics in self-assembled hybrid perovskite quantum wells. *ACS Nano* **2017**, *11*, 10834−10843.
(39) Gauthron, K.; Lauret, J.-S.; Doyennette, L.; Lanty, G.; Al Choueiry, A.; Zhang, S. J.; Brehier, A.; Largeau, L.; Mauguin, O.; Bloch, J.; et al. Optical spectroscopy of two-dimensional layered

DOI: 10.1021/acs.jpclett.8b03381
J. Phys. Chem. Lett. 2019, 10, 7−12

$(C_6H_5C_2H_4\text{-}NH_3)_2\text{-}PbI_4$ perovskite. *Opt. Express* **2010**, *18*, 5912−5919.
(40) Sangwan, V. K.; Lee, H. S.; Bergeron, H.; Balla, I.; Beck, M. E.; Chen, K. S.; Hersam, M. C. Multi-terminal memtransistors from polycrystalline monolayer molybdenum disulfide. *Nature* **2018**, *554*, 500−504.
(41) Guo, Y.; Saidi, W. A.; Wang, Q. 2D halide perovskite-based van der Waals heterostructures: contact evaluation and performance modulation. *2D Mater.* **2017**, *4*, No. 035009.
(42) Xiao, X.; Dai, J.; Fang, Y.; Zhao, J.; Zheng, X.; Tang, S.; Rudd, P. N.; Zeng, X. C.; Huang, J. Suppressed ion migration along the in-plane direction in layered perovskites. *ACS Energy Lett.* **2018**, *3*, 684−688.
(43) Li, D.; Wu, H.; Cheng, H. C.; Wang, G.; Huang, Y.; Duan, X. Electronic and ionic transport dynamics in organolead halide perovskites. *ACS Nano* **2016**, *10*, 6933−6941.
(44) Pan, D.; Fu, Y.; Chen, J.; Czech, K. J.; Wright, J. C.; Jin, S. Visualization and studies of ion-diffusion kinetics in cesium lead bromide perovskite nanowires. *Nano Lett.* **2018**, *18*, 1807−1813.
(45) Zhao, B.; Dang, W.; Liu, Y.; Li, B.; Li, J.; Luo, J.; Zhang, Z.; Wu, R.; Ma, H.; Sun, G.; et al. Synthetic control of two-dimensional NiTe2 single crystals with highly uniform thickness distributions. *J. Am. Chem. Soc.* **2018**, *140*, 14217−14223.
(46) Radisavljevic, B.; Radenovic, A.; Brivio, J.; Giacometti, V.; Kis, A. Single-layer MoS_2 transistors. *Nat. Nanotechnol.* **2011**, *6*, 147−150.
(47) Lin, Y. H.; Pattanasattayavong, P.; Anthopoulos, T. D. Metal-halide perovskite transistors for printed electronics: challenges and opportunities. *Adv. Mater.* **2017**, *29*, 1702838.
(48) Zhou, G.; Addou, R.; Wang, Q.; Honari, S.; Cormier, C. R.; Cheng, L.; Yue, R.; Smyth, C. M.; Laturia, A.; Kim, J.; et al. High-mobility helical tellurium field-effect transistors enabled by transfer-free, low-temperature direct growth. *Adv. Mater.* **2018**, *30*, 1803109.
(49) Li, D.; Cheng, H. C.; Wang, Y.; Zhao, Z.; Wang, G.; Wu, H.; He, Q.; Huang, Y.; Duan, X. The effect of thermal annealing on charge transport in organolead halide perovskite microplate field-effect transistors. *Adv. Mater.* **2017**, *29*, 1601959.
(50) Abbaszadeh, D.; Kunz, A.; Wetzelaer, G. A.; Michels, J. J.; Craciun, N. I.; Koynov, K.; Lieberwirth, I.; Blom, P. W. Elimination of charge carrier trapping in diluted semiconductors. *Nat. Mater.* **2016**, *15*, 628−633.
(51) Chin, X. Y.; Cortecchia, D.; Yin, J.; Bruno, A.; Soci, C. Lead iodide perovskite light-emitting field-effect transistor. *Nat. Commun.* **2015**, *6*, 7383.
(52) Li, D.; Cheng, H. C.; Wu, H.; Wang, Y.; Guo, J.; Wang, G.; Huang, Y.; Duan, X. Gate-induced insulator to band-like transport transition in organolead halide perovskite. *J. Phys. Chem. Lett.* **2017**, *8*, 429−434.
(53) Ghatak, S.; Pal, A. N.; Ghosh, A. Nature of electronic states in atomically thin MoS_2 field-effect transistors. *ACS Nano* **2011**, *5*, 7707−7712.
(54) Senanayak, S. P.; Yang, B.; Thomas, T. H.; Giesbrecht, N.; Huang, W.; Gann, E.; Nair, B.; Goedel, K.; Guha, S.; Moya, X.; et al.et. al Understanding charge transport in lead iodide perovskite thin-film field-effect transistors. *Science* **2017**, *3*, No. e1601935.
(55) Zhou, J.; Chu, Y.; Huang, J. Photodetectors based on two-dimensional layer-structured hybrid lead iodide perovskite semiconductors. *ACS Appl. Mater. Interfaces* **2016**, *8*, 25660−25666.
(56) Li, L.; Sun, Z.; Wang, P.; Hu, W.; Wang, S.; Ji, C.; Hong, M.; Luo, J. Tailored engineering of an unusual $(C_4H_9NH_3)_2(CH_3NH_3)_2Pb_3Br_{10}$ two-dimensional multilayered perovskite ferroelectric for a high-performance photodetector. *Angew. Chem., Int. Ed.* **2017**, *56*, 12150−12154.

DOI: 10.1021/acs.jpclett.8b03381
J. Phys. Chem. Lett. 2019, 10, 7−12